Supporting Information

Quasi-layer Co_2P-polarized Cu_3P nanocomposites with enhanced intrinsic interfacial charge transfer for efficient overall water splitting

Liangbin Liu#, Lei Ge#, Yuyang Sun, Binbin Jiang, Yafei Cheng, Lai Xu, Fan Liao, Zhenhui Kang*, Mingwang Shao**

Institute of Functional Nano & Soft Materials (FUNSOM), Jiangsu Key Laboratory for Carbon-Based Functional Materials & Devices, Soochow University, 199 Ren'ai Road, Suzhou, 215123, Jiangsu, PR China

* Correspondence to: xulai15@suda.edu.cn (L. Xu); zhkang@suda.edu.cn (Z. H. Kang); mwshao@suda.edu.cn (M. W. Shao).

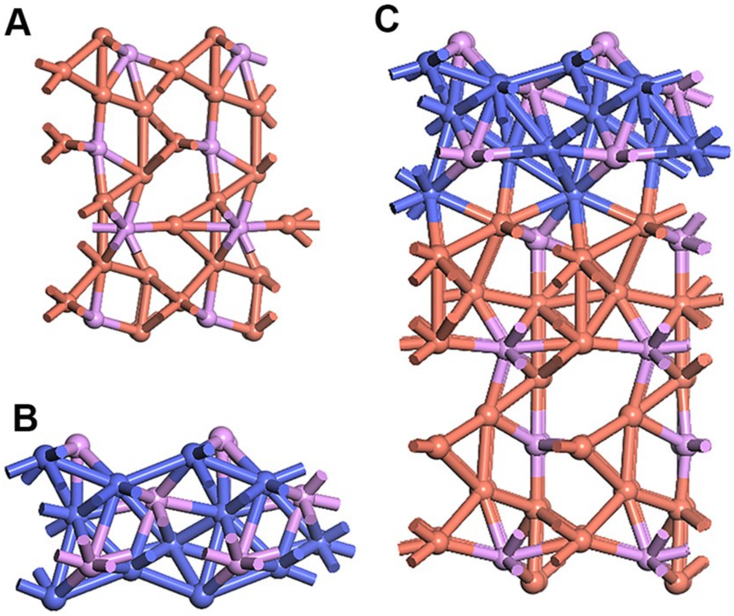

Figure S1. The supercell slabs of Cu_3P, Co_2P and $Cu_3P{\cdot}0.75Co_2P$. The nanocomposite was constructed by connecting the (001) surface of Cu_3P, and (001) surface of Co_2P.

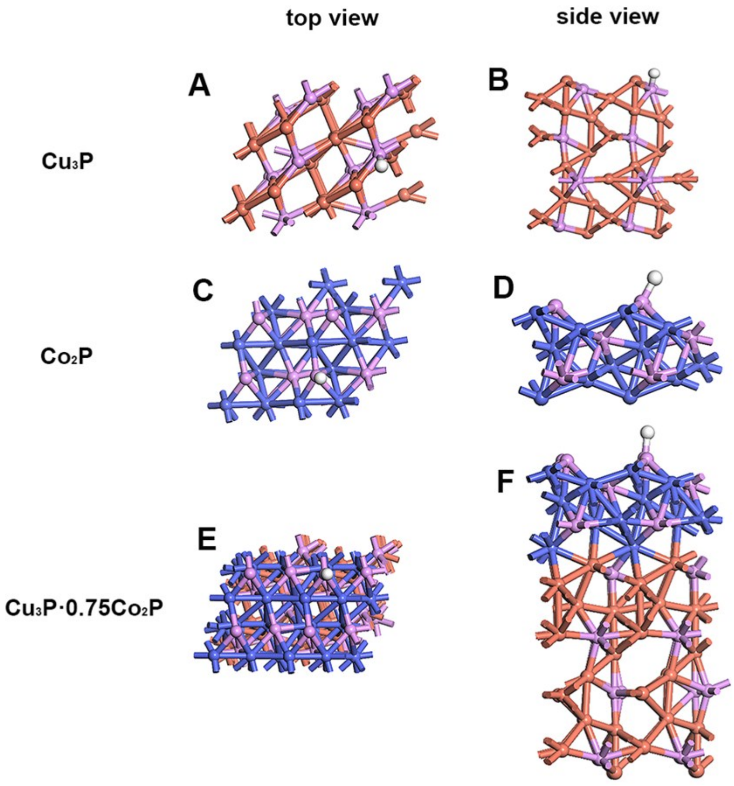

Figure S2. The configuration of H atom adsorption from top and side view of Cu_3P, Co_2P and $Cu_3P{\cdot}0.75Co_2P$.

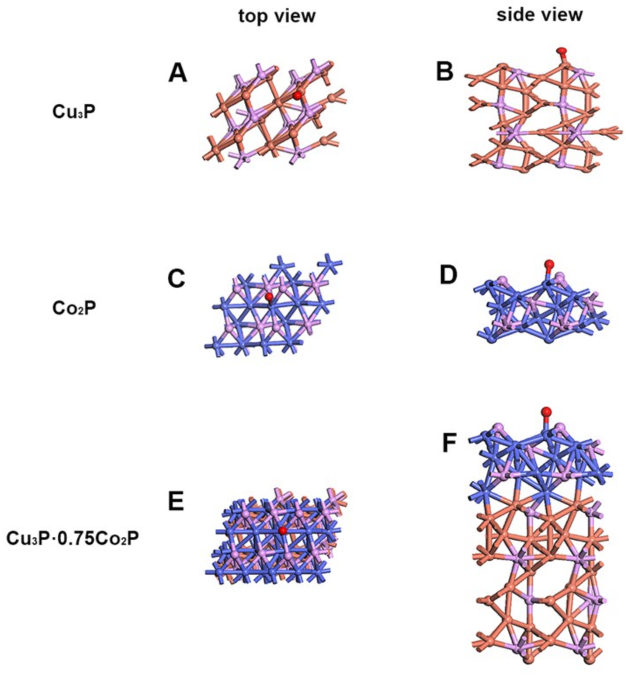

Figure S3. The configuration of O atom adsorption from top and side view of Cu_3P, Co_2P and $Cu_3P·0.75Co_2P$.

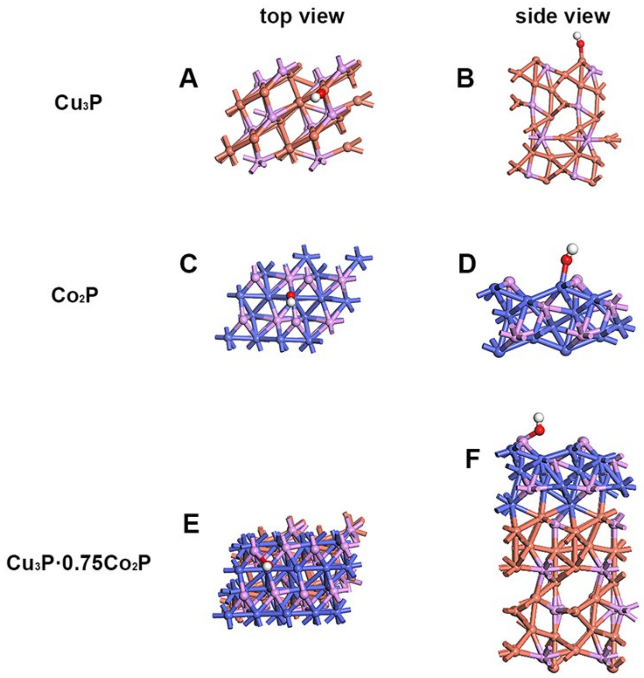

Figure S4. The configuration of OH atom adsorption from top and side view of Cu_3P, Co_2P and $Cu_3P \cdot 0.75Co_2P$.

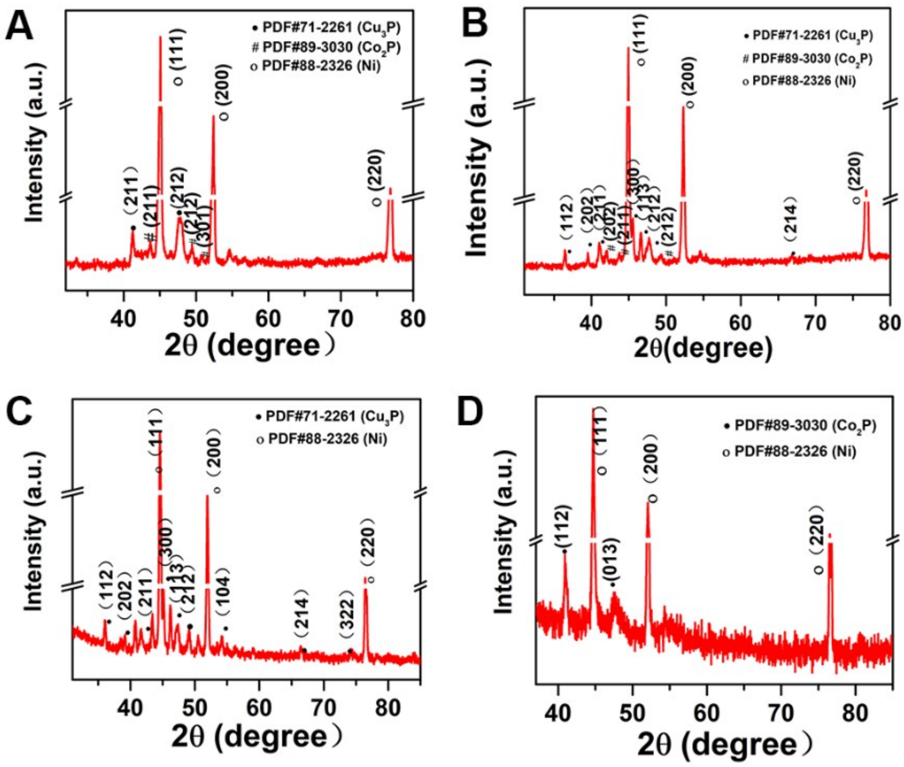

Figure S5. XRD patterns of (A) $Cu_3P{\cdot}1.5Co_2P$, (B) $Cu_3P{\cdot}0.375Co_2P$, (C) Cu_3P and (D) Co_2P on NF.

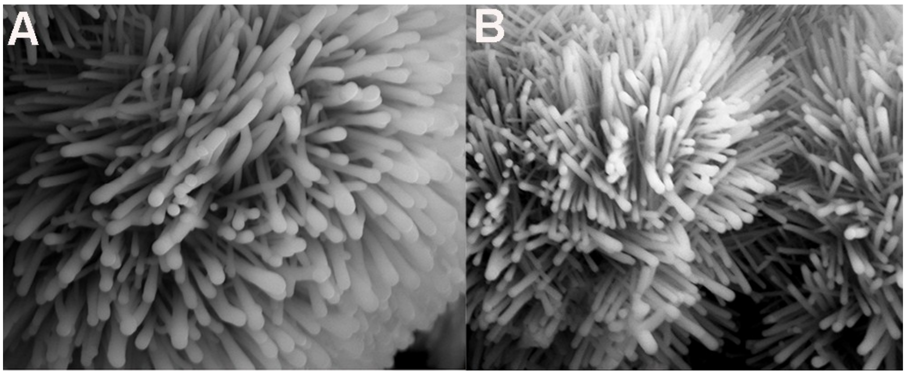

Figure S6. SEM images of (a) $Cu_3P{\cdot}1.5Co_2P$ (b) $Cu_3P{\cdot}0.375Co_2P$.

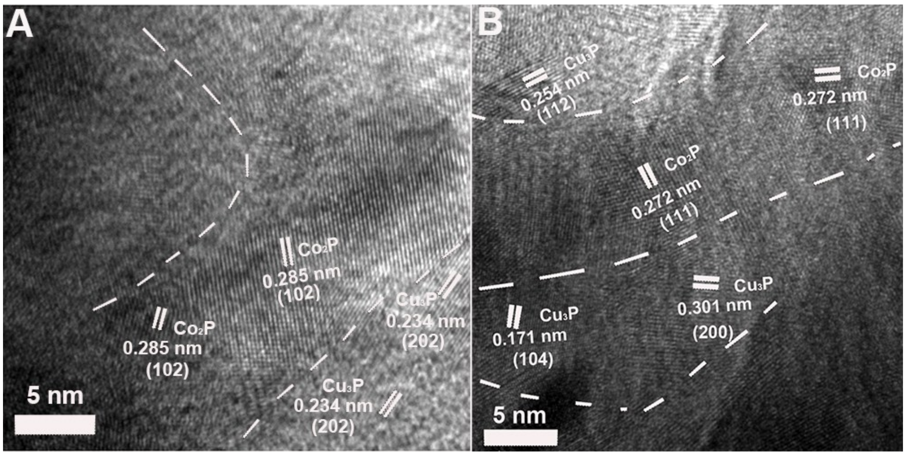

Figure S7. (A) and (B) are HRTEM images of numerous interfaces between Co_2P and Cu_3P.

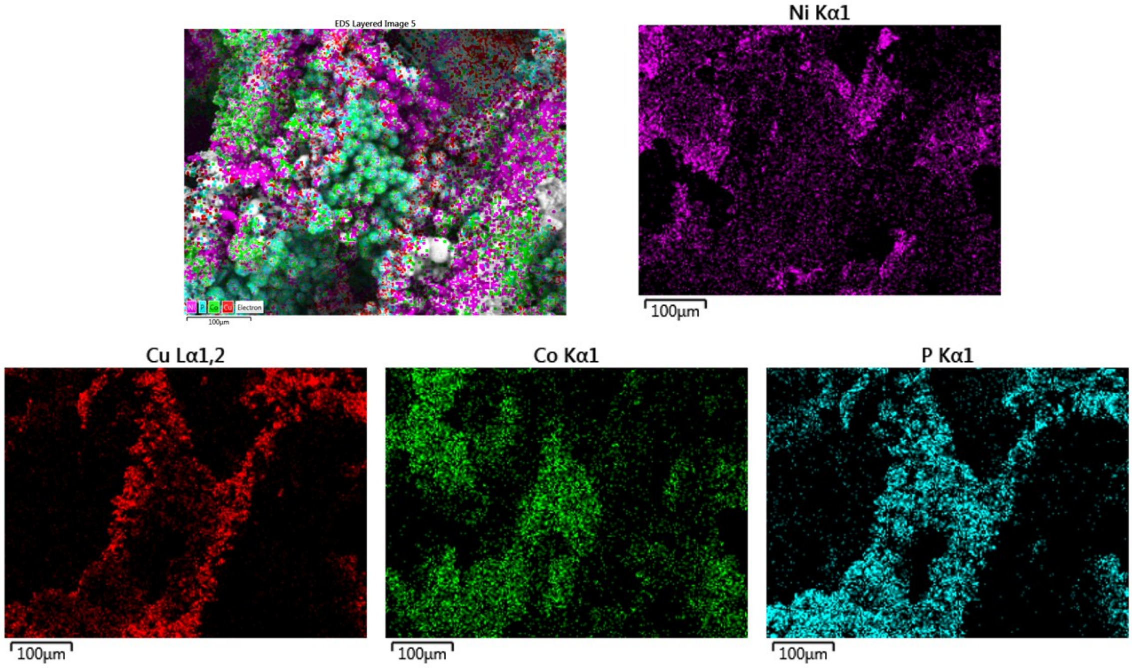

Figure S8. EDS mapping of the $Cu_3P{\cdot}0.75Co_2P$ formed on the Ni foam.

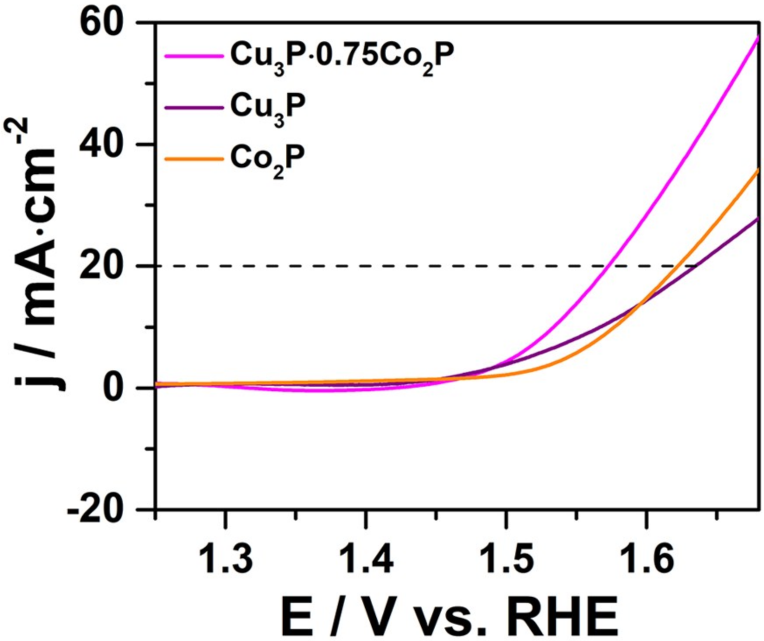

Figure S9. The LSV curves of Cu_3P/CC, Co_2P/CC and $Cu_3P\cdot0.75Co_2P$/CC measured in 1.0 M KOH solution.

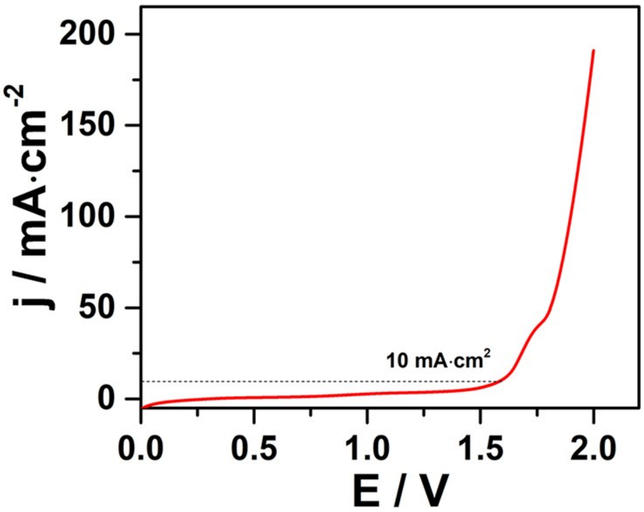

Figure S10. Water splitting in 1.0 M KOH for Pt/C and the IrO_2 electrodes in a two-electrode configuration.

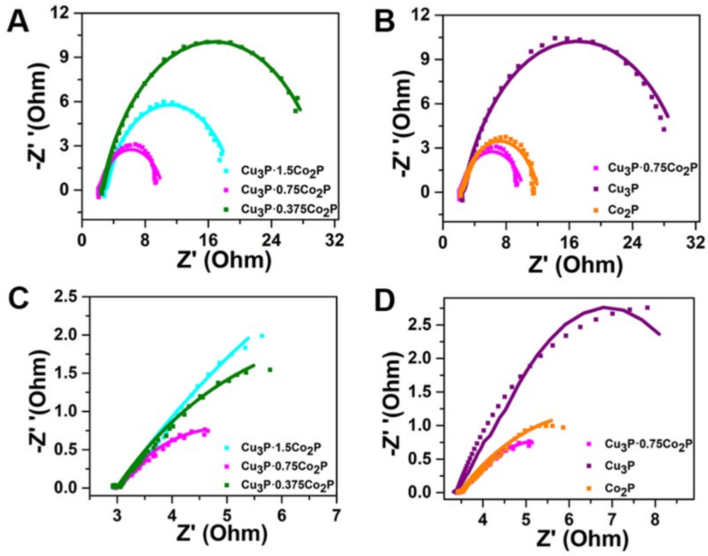

Figure S11. Nyquist plots of Cu_3P-Co_2P, Cu_3P and Co_2P in 1.0 M KOH at an applied potential of (A) and (B) HER at -0.125 V vs. RHE, and (C) and (D) OER at 1.437 V vs. RHE.

The cyclic voltammetry was tested of the Cu_3P·1.5Co_2P, Cu_3P·0.75Co_2P, Cu_3P·0.375Co_2P at the scan rates of 5-25 mV s^{-1} in Figures S3A, S3B and S3C. The C_{dl} was measured to evaluate the ECSA of each catalyst for HER (Figure S3D). The Cu_3P·0.75Co_2P possessed a 0.1598 mF cm^{-2} of ECSA, which was much larger than that of Cu_3P·0.375Co_2P (C_{dl} = 0.1078 mF cm^{-2}) and the Cu_3P·1.5Co_2P (C_{dl} = 0.1376 mF cm^{-2}). Figures S4A, S4B and S4C, shown the cyclic voltammetry of the Cu_3P·0.75Co_2P, Cu_3P and the Co_2P at the scan rates of 5-25 mV s^{-1}. The corresponding C_{dl} (Figure S4D) of the Cu_3P and the Co_2P are 0.0830 mF cm^{-2} and 0.0984 mF cm^{-2}, which are much smaller than the Cu_3P·0.75Co_2P. All of the ECSA information have illustrated that the Cu_3P·0.75Co_2P with a C_{dl}=0.1598 mF cm^{-2} is favorable to show higher electrocatalytic performance.

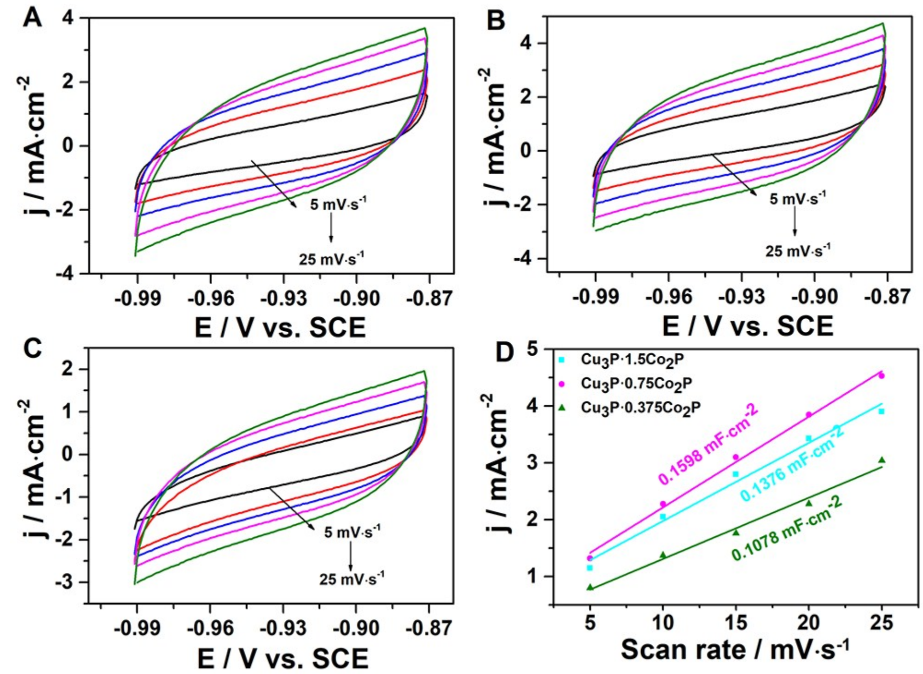

Figure S12. Cyclic voltammetry at scan rates of 5-25 mV s^{-1}: (A) Cu_3P·1.5Co_2P, (B) Cu_3P·0.75Co_2P, (C) Cu_3P·0.375Co_2P, in the range of -0.991--0.871 V vs. SCE in 1.0 M KOH medium; and (D) Charging current density differences (ΔJ = Ja - Jc) plotted against scan rates of the different ratios of Cu_3P-Co_2P nanocomposite. The linear slope, equivalent to twice the double-layer capacitance (C_{dl}).

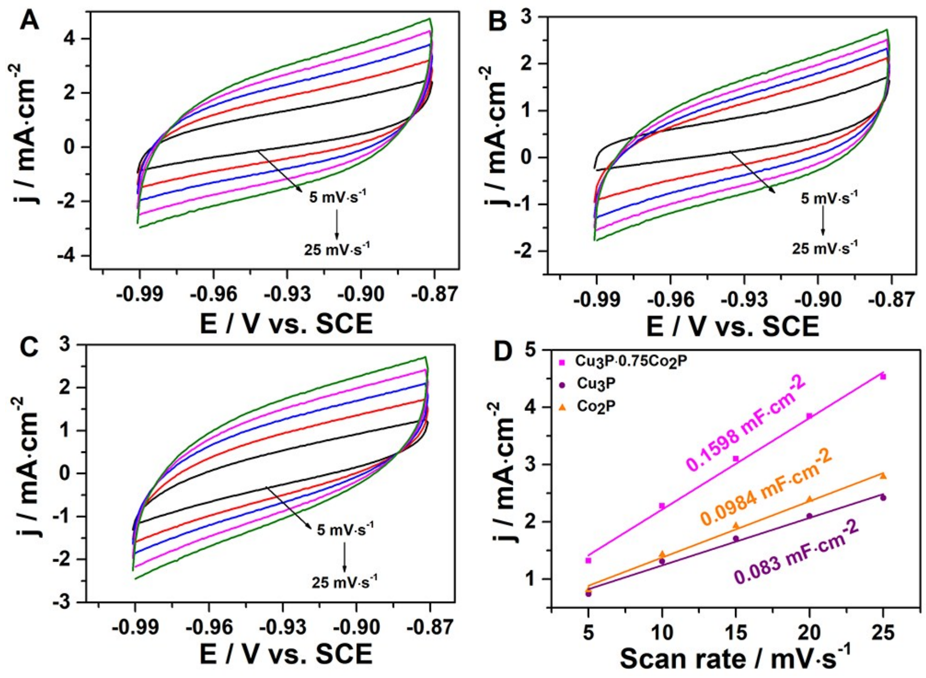

Figure S13. Cyclic voltammetry at scan rates of 5-25 mV s^{-1}: (A) $Cu_3P{\cdot}0.75Co_2P$, (B) Cu_3P and (C) Co_2P, in the range of -0.991--0.871 V vs. SCE in 1.0 M KOH medium. (D) Charging current density differences (ΔJ = Ja - Jc) plotted against scan rates of the different ratios of Cu_3P-Co_2P nanocomposite. The linear slope, equivalent to twice the double-layer capacitance (C_{dl}).

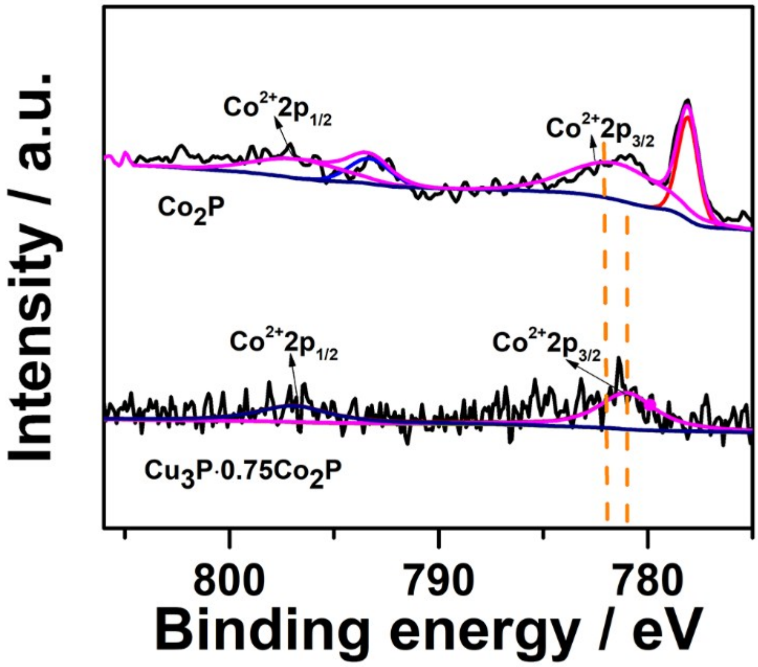

Figure S14. XPS spectra of Co 2p for $Cu_3P{\cdot}0.75Co_2P$ and Co_2P.

Figure S11 is the Co 2p spectra of $Cu_3P{\cdot}0.75Co_2P$ and Co_2P. For Co_2P, the binding energies at 778.1 eV for Co $2p_{3/2}$ and 793.3 eV for Co $2p_{1/2}$ are spin-orbit characteristics of Co, while the existing binding energies at 782.1 eV for Co^{2+} $2p_{3/2}$ and 797.1 eV are spin-orbit characteristics of Co^{2+}. While for $Cu_3P{\cdot}0.75Co_2P$, the peaks at 781.6 eV for Co^{2+} $2p_{3/2}$ and 796.8 eV for Co^{2+} $2p_{1/2}$ are spin-orbit characteristics of Co^{2+}. The comparation of Co 2p spectra between $Cu_3P{\cdot}0.75Co_2P$ and Co_2P shows that there is a negative shift of 0.5 eV for $Cu_3P{\cdot}0.75Co_2P$ contrasted to the Co^{2+} of the Co_2P.

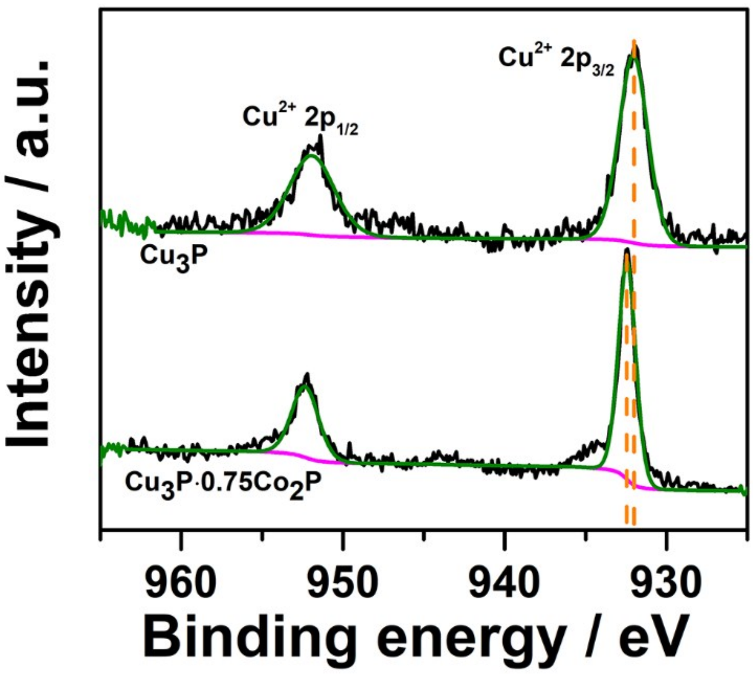

Figure S15. XPS spectra of Cu 2p for $Cu_3P·0.75Co_2P$ and Cu_3P.

Figure S12 is the core spectra of Cu 2p. For Cu_3P catalyst, the peaks at 931.9 eV and 951.9 eV are assigned to the Cu^{2+} $2p_{3/2}$ and Cu^{2+} $2p_{1/2}$ of the Cu_3P. In terms of $Cu_3P·0.75Co_2P$, the Cu 2p shows two typical peaks of 932.3 eV and 952.3 eV that are associated with Cu^{2+} $2p_{3/2}$ and Cu^{2+} $2p_{1/2}$, respectively. Comparing with the Cu 2p spectrum of the Cu_3P, the Cu^{2+} of the $Cu_3P·0.75Co_2P$ has a positive shifting of 0.4 eV. Figures S10 and S11 indicate there is charge transfer from Cu_3P to Co_2P.

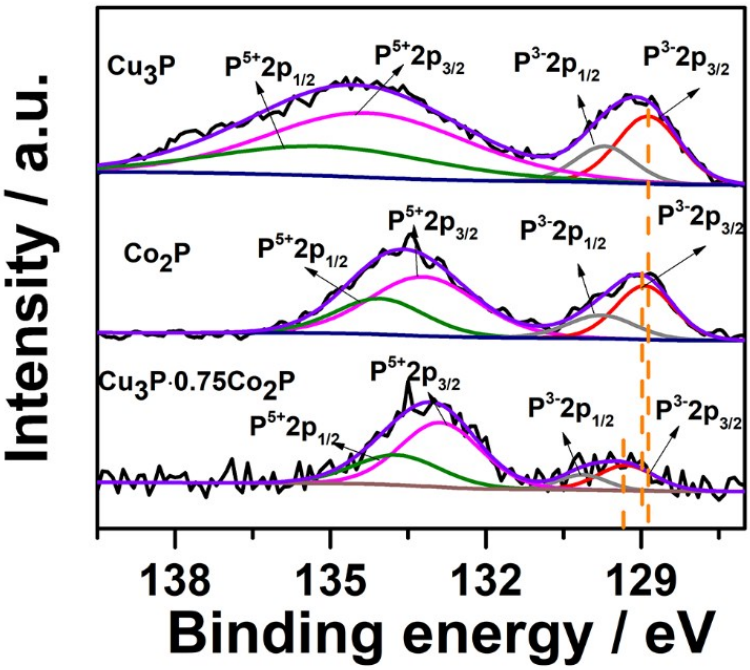

Figure S16. XPS spectra of P 2p for $Cu_3P\cdot0.75Co_2P$, Co_2P and Cu_3P.

Figure S13 is the P 2p spectra of $Cu_3P\cdot0.75Co_2P$, Co_2P and Cu_3P. For Cu_3P, the P^{3-} $2p_{3/2}$ and P^{3-} $2p_{1/2}$ are shown at the peak position of 128.8eV and 129.7eV. While the 134.3eV and the 135.2eV are corresponding to the P^{5+} $2p_{3/2}$ and P^{5+} $2p_{1/2}$. For Co_2P, the P^{3-} $2p_{3/2}$ has a distinct peak at 128.9 eV, a matching peak of 129.8 eV ascribed to P^{3-} $2p_{1/2}$. The peaks at 133.2 eV and the other of 134.1 eV, corresponding to the spin-orbit characteristics of P^{5+} $2p_{3/2}$ and P^{5+} $2p_{1/2}$, respectively. As to the $Cu_3P\cdot0.75Co_2P$, the corresponded 129.3 eV and 130.2 eV of are the typical peaks of the P^{3-} $2p_{3/2}$ and the P^{3-} $2p_{1/2}$, which has a positive shift of 0.4 eV compared with the P^{3-} of the Cu_3P

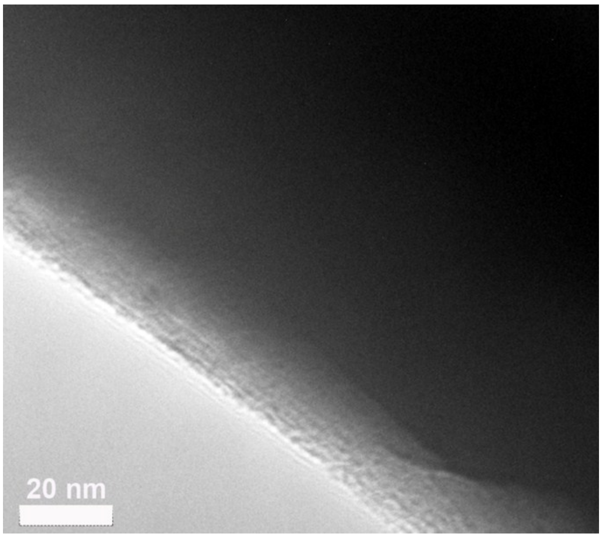

Figure S17. TEM image of the $Cu_3P{\cdot}0.75Co_2P$ anode catalyst after the stability test, showing a thick layer on its surface due to oxidation process in OER.

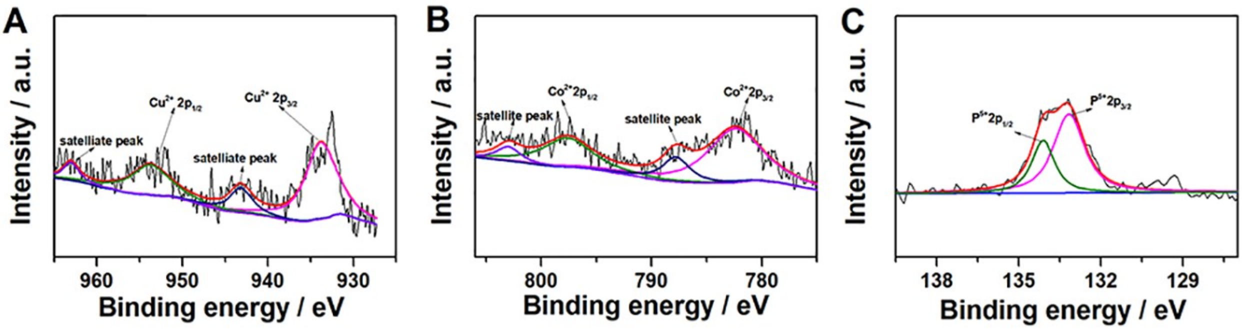

Figure S18. XPS spectra of Cu 2p, Co 2p and P 2p for $Cu_3P{\cdot}0.75Co_2P$ anode catalyst after the stability test.

Table S1. The calculation of the adsorption free energy for the pure Co_2P, the pure Cu_3P and the $Cu_3P{\cdot}0.75Co_2P$ nanocomposite.

Materials	ΔE_H(eV)	ΔE_{OH}(eV)	ΔE_O(eV)
Co_2P	0.065	0.063	0.556
Cu_3P	0.633	2.298	-0.146
$Cu_3P{\cdot}0.75Co_2P$	-0.386	1.453	-0.488

Table S2. The TOF values of the catalysts.

	$Cu_3P·1.5Co_2P$	$Cu_3P·0.75Co_2P$	$Cu_3P·0.375Co_2P$
TOF(H_2 s^{-1})	1.67×10^{-4}	3.58×10^{-4}	3.12×10^{-4}

The TOF value is determined by the following equation, in order to assess the efficiency of the catalysts. TOF = $n_{(H2)}$ / n_{cata} s, where $n_{(H2)}$ is the molal weight of the hydrogen, s is the time, and n_{cata} is the moral weight of the catalysts.

Table S3. Comparison of recent bifunctional electrocatalysts for overall water splitting in 1.0 M KOH.

Catalyst	Overall voltage for j = 10 mA cm^{-2}	Reference
$Cu_3P{\cdot}0.75Co_2P$	1.55 V	*This work*
NF-Ni_3Se_2/Ni	1.612 V	*Nano Energy, 2016, 24, 103.*
NiFe/$NiCo_2O_4$	1.67 V	*Adv. Funct. Mater.* 2016, *26,* 3515.
NiCoP NPs	1.64 V	*Adv. Mater. Interfaces, 2015, 3, 1500454*
Co-P	1.65 V	*Angew. Chem. Int. Ed.* 2015, *54,* 6251.
CoP	1.62 V	*Adv. Funct. Mater., 2015, 25, 7337.*
$Ni_{0.9}Fe_{0.1}$/NC	1.68 V	*J. Am. Chem. Soc., 2015, 137, 2688.*
EG/$Co_{0.85}$Se/NiFe-LDH	1.67 V	*Energy Environ. Sci., 2016, 9, 478.*
Ni_5P_4	1.7 V	*Angew. Chem. Int. Ed. 2015, 54.*
CoP/rGO	1.7 V	*Chem. Sci., 2016, 7, 1690.*